

Article

# An Ultrathin Low-Profile Tightly Coupled Dipole Array Fed by Compact Zigzagging Baluns

Weiwei Wu , Yuchen Yan , Shaozhi Wang, Yuhong Ma and Naichang Yuan

State Key Laboratory of Complex Electromagnetic Environment Effects on Electronics and Information System, School of Electronic Science, National University of Defense Technology, #109, Deya Road, Changsha 410073, China; yanyuchenyc@nudt.edu.cn (Y.Y.); wangshaozhi@nudt.edu.cn (S.W.); mazaizainudt@outlook.com (Y.M.); yuannaichang@hotmail.com (N.Y.)

\* Correspondence: wuweiwei@nudt.edu.cn; Tel.: +86-180-7317-0416

**Abstract:** In this paper, we propose for the first time a novel feed approach to a tightly coupled dipole array (TCDA). Firstly, compact zigzagging microstrip feedlines are utilized as baluns to feed our array elements to obtain wideband impedance-matching characteristics. Secondly, this array is designed on ultrathin substrates aiming at obtaining ultra-tight coupling between the dipole arms of two neighboring elements. Some irreplaceable parasitic pads are developed and added to the radiating arms to improve both the impedance and radiation characteristics of the TCDA. With these technologies, a  $12 \times 12$  TCDA prototype is designed, fabricated and measured for verification. The array achieves an impressive impedance bandwidth spanning of 4–18 GHz for  $S_{11} < -10$  dB. Its radiation patterns and realized gain are measured to verify its stable electromagnetic characteristics. Its realized gain is from 15 dB to 25 dB within the operating frequency band. Its efficiency is around 91%. Its measured results show good agreement with simulations.

**Keywords:** phased arrays; tightly coupled arrays; antenna feeds; balun; impedance matching



**Citation:** Wu, W.; Yan, Y.; Wang, S.; Ma, Y.; Yuan, N. An Ultrathin Low-Profile Tightly Coupled Dipole Array Fed by Compact Zigzagging Baluns. *Electronics* **2023**, *12*, 2752. <https://doi.org/10.3390/electronics12122752>

Academic Editor: Paolo Baccarelli

Received: 29 May 2023

Revised: 14 June 2023

Accepted: 18 June 2023

Published: 20 June 2023



**Copyright:** © 2023 by the authors. Licensee MDPI, Basel, Switzerland. This article is an open access article distributed under the terms and conditions of the Creative Commons Attribution (CC BY) license (<https://creativecommons.org/licenses/by/4.0/>).

## 1. Introduction

Wideband antennas and phased arrays become the subject of strong interest when the antenna platforms of radars, communications, remote-sensing, etc., shrink their sizes greatly. These wideband arrays are required to cover a wideband operating frequency band, produce multiple beams, have wide-angle scanning, and so on. In 1965, Wheeler proposed a phased-array antenna made of an infinite current sheet [1,2]. As a practical realization of Wheeler's current sheet antenna (CSA) array, tightly coupled dipole arrays (TCDAs) [3–42] are attractive candidates to meet these challenging requirements for wideband arrays. Instead of avoiding the capacitive coupling between neighboring antenna elements of traditional arrays, one TCDA utilizes the interelement coupling to achieve many desirable properties, such as wide impedance and pattern bandwidth, a very low profile in cross section, layered planar structure compatible with conformal applications, etc. [3] (p. 448). In this way, TCDAs achieve wideband impedance matching and wide-angle scanning with their low-profile natures. The integration of multiple antennas into a low-profile tightly coupled dipole phased array on one antenna platform offers the potential of size, weight and power reductions. There have been numerous investigations into improving the performance of TCDAs. Firstly, some researchers have presented many novel antenna element configurations [4–15]. A kind of magneto-electric (ME) dipole structure [4,5] has been developed for TCDAs. Some two-dimensional planar arms [6–10] for TCDAs have been designed. Furthermore, some three-dimensional vibrators [11–15] have been illustrated. Secondly, creative feeding structures [16–21] have been introduced. A kind of Marchand balun with comb-type perforated structure [16] has been reported. A feed structure with a gamma-shaped probe [17] has been presented. A novel differential feed structure [18] has been expanded. Thirdly, wide-angle impedance-matching (WAIM) structures [22–31]

have been developed. Many new meta-surfaces have been designed as two-dimensional WAIMs [22–28]. Vertically directive metamaterials have been utilized as three-dimensional WAIMs [29–31]. Fourthly, the ground structures have been optimized to improve the electromagnetic characteristics of TCDA. On the one hand, some sorts of specially shaped frequency-selective surfaces [32–35] have been applied to the ground structures. On the other hand, the ground structures have been loaded with resistive frequency-selective structures [36,37] or magnetic frequency-selective structures [38]. Finally, some efficient design methods [39–42] for TCDA have been presented.

In this paper, we propose an ultrathin low-profile tightly coupled dipole array. First of all, to realize the impedance matching between the feeding coaxial lines and the dipole antennas, novel compact zigzagging feedlines are developed as a balun to improve the TCDA's feed performance. Secondly, the thickness of the substrates for this TCDA is only 0.127 mm to enhance the capacitive coupling between neighboring elements. Three pairs of parasitic pads with different dimensions are loaded to each dipole arm to further enhance the capacitive coupling between neighboring antenna elements over a wide frequency band. Based on these approaches, the balun design becomes simple and the capacitive coupling between neighboring elements is greatly increased. Since our TCDA is developed without WAIM, the profile of this configuration is lowered.

This paper is organized as follows. Section 2 presents the design methodology and details of the TCDA element and the proposed array. Section 3 introduces the fabrication and measurements of a  $12 \times 12$  array prototype. The impedance and radiation performances are expanded and discussed in detail to verify the design. In the end, conclusions are drawn in Section 4.

## 2. Design of the Proposed Array

### 2.1. Design of Compact Zigzagging Feedlines

Admittedly, the straight-and-parallel-strip-to-microstrip transition line is the easiest way to feed two dipole arms etched separately on the two sides of one dielectric substrate. The microstrip line is connected to a  $50 \Omega$  standard coaxial cable feed. The two parallel strip lines are attached to the nearly  $200 \Omega$  dipole arms.

The characteristic impedance of the straight and parallel strip line is given by [43] (pp. 429–433):

$$Z_0 = \frac{d}{w} \sqrt{\frac{\mu}{\epsilon}} = \sqrt{\frac{L}{C}} \quad (1)$$

where  $d$  is the distance between these two straight and parallel strip lines and  $w$  is the width of each parallel strip line.  $L$  is the inductance per unit length of the parallel strip line and  $C$  is the capacitance per unit length of the parallel strip line. The inductance is calculated by:

$$L = \mu \frac{d}{w} \text{ (H/m)} \quad (2)$$

The capacitance is calculated by:

$$C = \epsilon \frac{w}{d} \text{ (F/m)} \quad (3)$$

As shown in Figure 1, to achieve a  $200 \Omega$  characteristic impedance, the two parallel strip lines should apparently be separated widely, which means that the distance  $d$  is large, or the width of each line  $w$  should become ultra-small. Considering the fabrication limitation, the minimum value of the width  $w$  can only be set to 0.1 mm. It is hard to reach an ultra-small value for the width  $w$  under the methods of fabrication considered. Thus, the distance  $d$  between the two parallel strip lines is studied and optimized, aiming to increase its characteristic impedance. The value of  $d$  can be adjusted along the  $x$  direction or along the  $y$  direction or both, since  $d = \sqrt{d_x^2 + d_y^2}$ . Because the strip lines are separately etched on the top and bottom layer, the distance  $d_y$  is equal to the thickness of the dielectric substrate

and is fixed. Instead, the distance  $d$  between two parallel strip lines can be adjusted along the  $x$  direction, which is  $d_x$ . Figure 1a shows the configuration of the strip lines when  $d_x = 0$  and  $d_y \neq 0$ . Figure 1b presents the case when  $d_x \neq 0$  and  $d_y \neq 0$ .

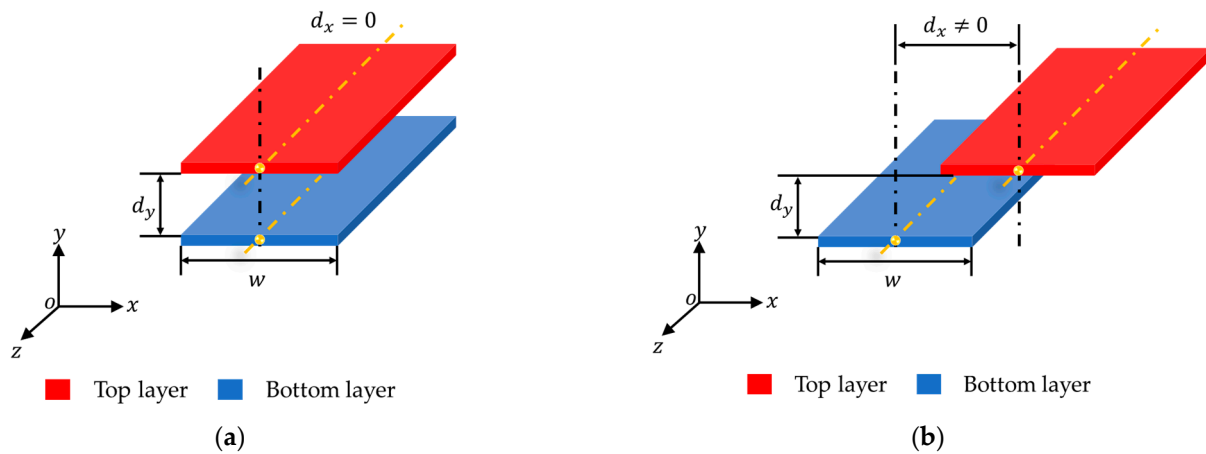


**Figure 1.** The configurations of straight and parallel strip lines. (a)  $d_x = 0$  and  $d_y \neq 0$ . (b)  $d_x \neq 0$  and  $d_y \neq 0$ .

Based on the analysis above, in our design, the strip lines are no longer straight and parallel. They become zigzagging strip lines to increase  $d_x$  and finally to obtain high impedance  $Z_0$ . Compared with the straight and parallel strip lines with the same electromagnetic properties, this kind of zigzagging line is shorter. Thus, this novel zigzagging-strip-lines-to-microstrip-lines transition structure is called a compact zigzagging balun (CZB), depicted in Figure 2. The red region is etched on the top layer of the substrate with a thickness  $t = 0.127$  mm and relative dielectric constant  $\epsilon_r = 2.2$ . The blue one is etched on the bottom layer. The zigzagging strip lines consist of eight sections. Two neighboring sections, sec  $i - 1$  and sec  $i$ , are zoomed in and displayed in Figure 2. Each section has two straight and parallel strip lines (SPSLs) etched separately on the top and bottom layers. The distance between these two lines along the  $x$  direction is  $d_x^i$  ( $i = 1, 2, \dots, 8$ ). It is studied and illustrated in detail later. Each SPSL connects to two oblique lines (OLs) along the  $z$  direction. The SPSLs have the same length,  $l_p$ . The oblique lines of two neighboring sections connect with each other to form transition cross lines. The length of the cross lines along the  $z$  direction is  $l_c$ . Comparatively, the location of the frequency band on the spectrum is more sensitive to the length  $l_c$  than the length  $l_p$ . When  $l_c$  is increased, the whole operating band moves towards the lower frequency area. To achieve a low-profile antenna array, it is better to keep these two lengths  $l_p$  and  $l_c$  as short as possible once the frequency band meets requirements.

The distance  $d_y$  between two SPSLs along the  $y$  axis is fixed and equals the thickness of the substrate, which is 0.127 mm. To obtain a large characteristic impedance  $Z_0$ ,  $d_x^i$  ( $i = 1, 2, \dots, 8$ ) can be gradually enlarged as the superscript index  $i$  increases to raise the inductance in Equation (2) and reduce the capacitance in Equation (3) at the same time, as shown in Figure 2. It is the key parameter to adjust the characteristic impedance of the zigzagging strip lines. When  $d_x^i$  is gradually increased from Section 1 to Section 8, the impedance is transformed from  $50 \Omega$  at port1 to  $200 \Omega$  at port2 within a wide frequency band.

Port1 is connected to a  $50 \Omega$  standard coaxial cable feed. Port2 is attached to the  $200 \Omega$  dipole arms. The CZB realizes two functions: the impedance transforming from  $50 \Omega$  to  $200 \Omega$  and from the unbalanced microstrip line to the balanced dipole arms. The optimized dimensional parameters are given by Table 1 below.

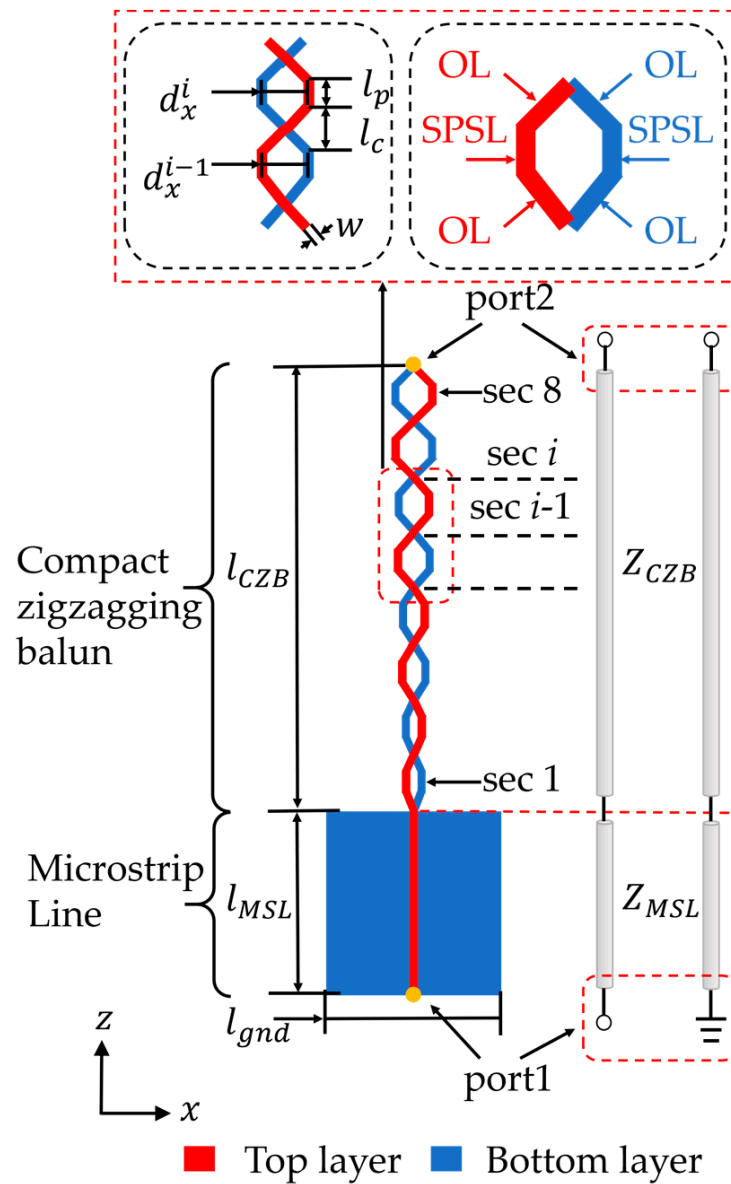


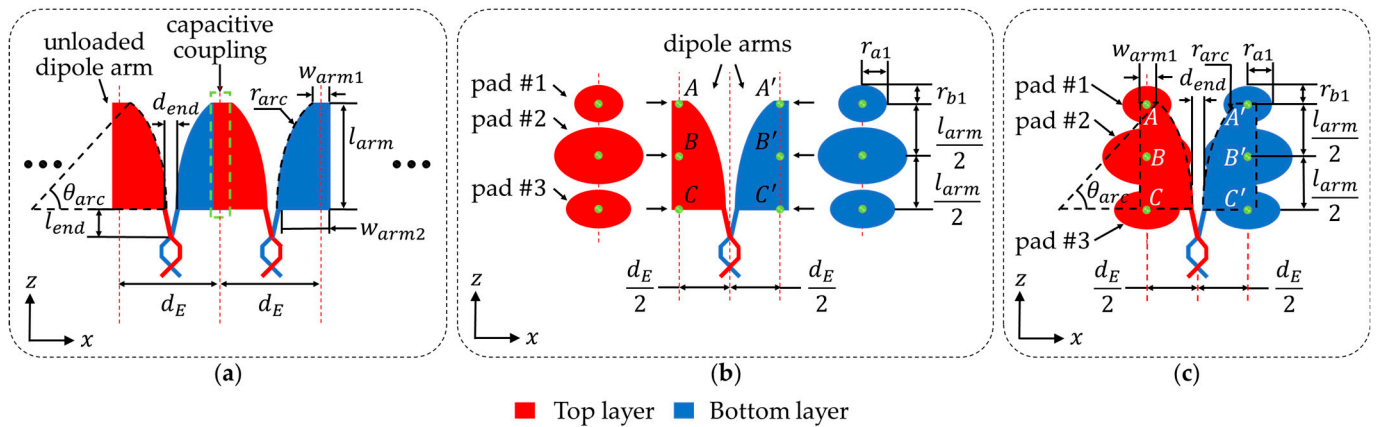
Figure 2. The compact zigzagging balun (CZB).

Table 1. Dimensions of the CZB (Units: mm).

Dimension Parameter	Value	Dimension Parameter	Value
$l_{gnd}$	5	$l_{MSL}$	5
$l_c$	1	$l_p$	0.5
$l_{CZB}$	12	$d_x^1 = d_x^2$	0.4
$d_x^3 = d_x^4$	0.5	$d_x^5 = d_x^6$	0.6
$d_x^7 = d_x^8$	0.7	$w$	0.2

### 2.2. Design of Pad-Loaded Dipole Arms

In consideration of avoiding the grating lobes over a wide frequency band, the distance between two neighboring antenna elements has to be small. For this reason, the dipole arms from these two elements cannot have enough area for capacitive coupling enhancement. Figure 3a shows this sort of commonly unloaded dipole arm of a TCDA, which is fed by the CZB.



**Figure 3.** The evolution of the proposed dipole arms: (a) the original unloaded dipole arms of a TCDA; (b) the unloaded dipole arms and three pairs of pads; (c) the loaded dipole arms of a TCDA.

To solve this problem, three pads (pad #1~pad #3) are loaded to each dipole arm to increase the coupling between two neighboring dipole arms which are separately located on the top and bottom layers. The dipole arms before pad loading and after pad loading are depicted in Figure 3b,c.

The centers of pad #1~#3 are correspondingly located at points A, B and C on the top layer. The other three centers of pad #1'~#3' on the bottom layer are separately located at points A', B' and C'. The distances  $d_{AB}$ ,  $d_{BC}$ ,  $d_{A'B'}$  and  $d_{B'C'}$  along the z direction are all equivalent to  $l_{arm}/2$ . The major and minor axes of each elliptic pad #i or pad #i' are separately represented by  $r_{ai}$  and  $r_{bi}$ ,  $i = 1, 2, 3$ .

Finally, part of our three-dimensional proposed TCDA is shown in Figure 4a and the equivalent circuit for one antenna element is expanded in Figure 4b. Slots are cut on the metallic ground plane. The 0.127-mm-thick dielectric substrate of each linear TCDA is vertically inserted into the slots. To obtain a better view, the substrate is hidden.

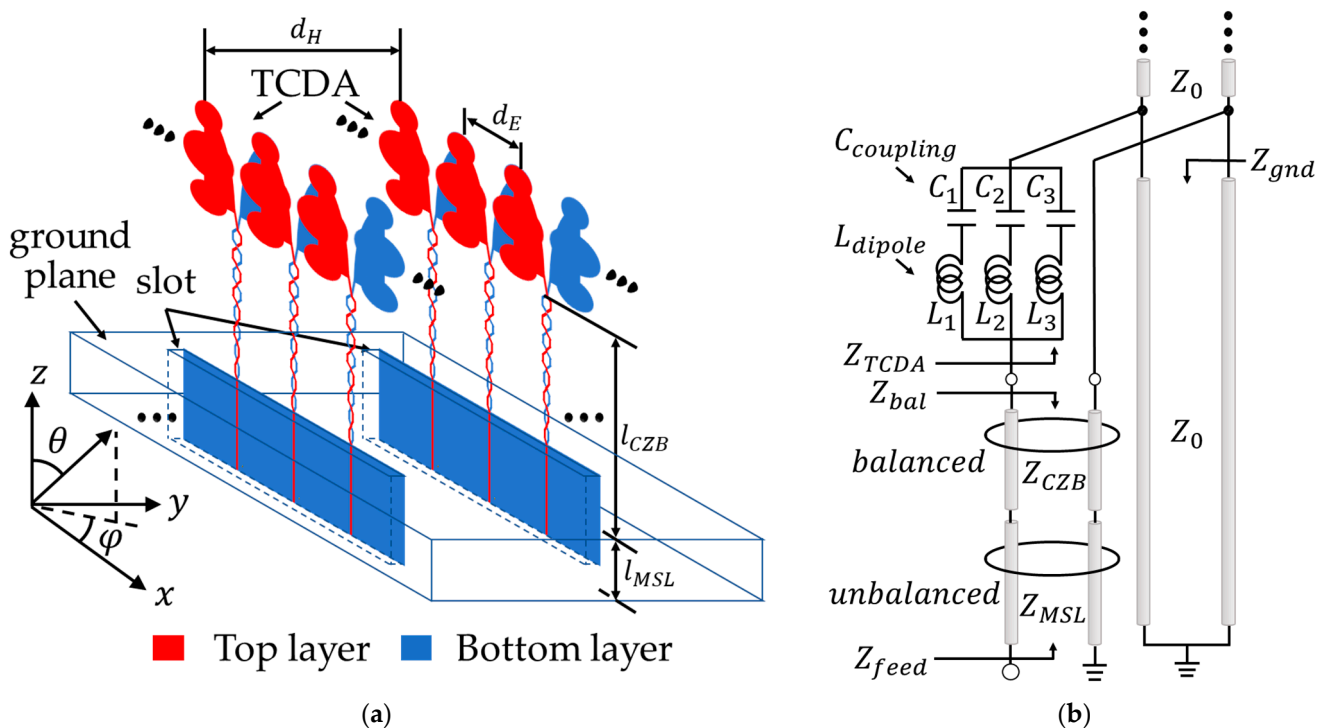


**Figure 4.** Part of our three-dimensional proposed TCDA: (a) part of three-dimensional proposed TCDA; (b) the equivalent circuit model of one antenna element.

Table 2 presents all the optimized parameters of the loaded-pad TCDA shown in Figures 3 and 4. The curve outline of each dipole arm is one arc of a circle with the radius  $r_{arc} = 15$  mm and the angle  $\theta_{arc} = 40^\circ$ , shown in Figure 3.  $d_E$  is the E-plane ( $x$ -dimension) element spacing, and  $d_H$  is the H-plane ( $y$ -dimension) element spacing, shown in Figure 4a.

**Table 2.** Dimensions of the TCDA (Units: mm).

Dimension Parameter	Value	Dimension Parameter	Value
$l_{arm}$	9.5	$w_{arm1}$	0.7
$w_{arm2}$	4	$d_E$	8
$d_H$	8	$\theta_{arc}$	$40^\circ$
$l_{end}$	1.7	$d_{end}$	0.6
$r_{a1}$	2.5	$r_{b1}$	2
$r_{a2}$	3.5	$r_{b2}$	2
$r_{a3}$	3.2	$r_{b3}$	2

The equivalent circuit model of the loaded-pad TCDA is described by Figure 4b. The pads and the loaded dipole arm consists of three pairs of LC circuits.  $C_{coupling}$  and  $L_{dipole}$  consist of  $C_i (i = 1, 2, 3)$  and  $L_i (i = 1, 2, 3)$ , respectively. On the one hand, the TCDA is loaded by the ground plane which is represented by a short-circuit transmission line. The input impedance of this transmission line  $Z_{gnd}$  is given by [43] (p. 455):

$$Z_{gnd} = jZ_0 \tan \beta l \tag{4}$$

where  $Z_0$  and  $\beta$  are the characteristic impedance and the propagation constant of the dielectric substrate. The spacing between the dipole arms and the ground plane is  $l = l_{CZB}$ . The propagation constant for this line is given by [42] (p. 4539):

$$\beta = k_0 \sqrt{\epsilon_r} \cos \theta \tag{5}$$

where  $k_0$  is the free space wavenumber, and  $\epsilon_r$  is the relative permittivity of the substrate. The scan angle  $\theta$  is illustrated in Figure 5.

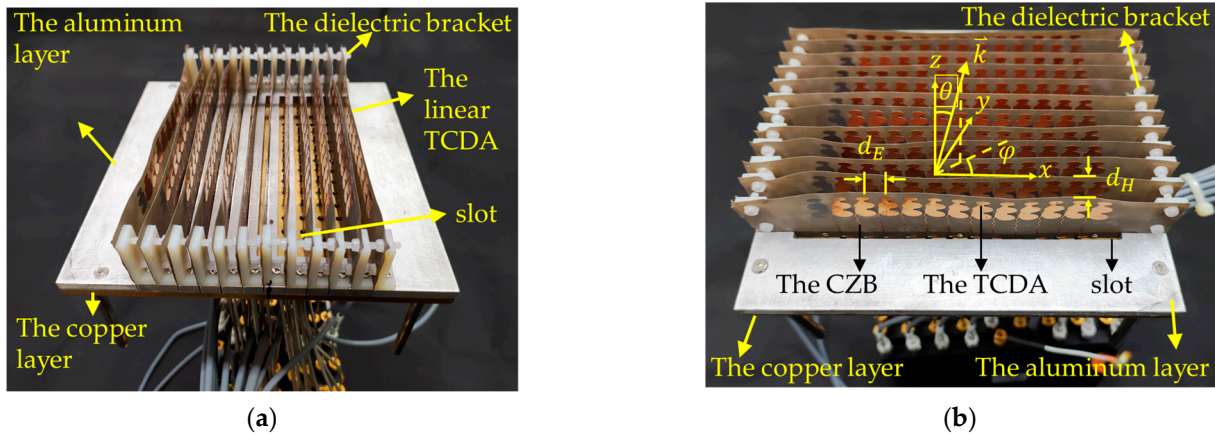


**Figure 5.** Photograph of the manufactured  $12 \times 12$  TCDA prototype. (a) Side view of the TCDA. (b) The antenna elements with their CZB.

The TM mode is excited when scanning in the E-plane ( $\varphi = 0^\circ$ ) and the TE mode is excited when scanning in the H-plane ( $\varphi = 90^\circ$ ). The characteristic impedance of transmission line  $Z_0^{TM}$  and  $Z_0^{TE}$  in Figure 6 when scanning in the E-plane and H-plane is given by [42] (p. 4539):

$$Z_0^{TM} = \eta \sqrt{\frac{\mu_r}{\epsilon_r} \frac{d_E}{d_H} \cos \theta} \tag{6}$$

$$Z_0^{TE} = \eta \sqrt{\frac{\mu_r}{\epsilon_r}} \frac{d_E}{d_H \cos\theta} \quad (7)$$

where  $\eta = 377 \Omega$  is the characteristic impedance of free space. When  $\theta = 0^\circ$  and  $d_E = d_H = 8 \text{ mm}$ , there is no scanning and the characteristic impedances  $Z_0^{TM}$  and  $Z_0^{TE}$  are the same,  $Z_0 = Z_0^{TM} = Z_0^{TE} = 254 \Omega$ . The input impedance of the short-circuit transmission line  $Z_{gnd}$  is  $Z_{gnd} = jZ_0 \tan\beta l_{CZB} = j7 \Omega$  at 8.5 GHz. The L-C circuit with  $C_{coupling}$  and  $L_{dipole}$  is designed to raise the operating bandwidth of the TCDA:  $L_1 = 57.7 \text{ nH}$ ,  $C_1 = 0.075 \text{ pF}$ ;  $L_2 = 60.4 \text{ nH}$ ,  $C_2 = 0.11 \text{ pF}$ ;  $L_3 = 28.2 \text{ nH}$ ,  $C_3 = 78.3 \text{ pF}$ . Following this, the input impedance of the TCDA is  $Z_{TCDA} = Z_0 = 254 \Omega$ . Meanwhile, the TCDA is connected to the coaxial feedline by a balun. The impedance of the coaxial feedline  $Z_{feed}$  is  $Z_{feed} = 50 \Omega$ . The impedance of the unbalanced microstrip line  $Z_{MSL}$  is  $Z_{MSL} = 75 \Omega$ . The terminal impedance of the CZB  $Z_{bal}$  is  $Z_{bal} = 254 \Omega$ , which matches the input impedance of the TCDA  $Z_{TCDA}$ .

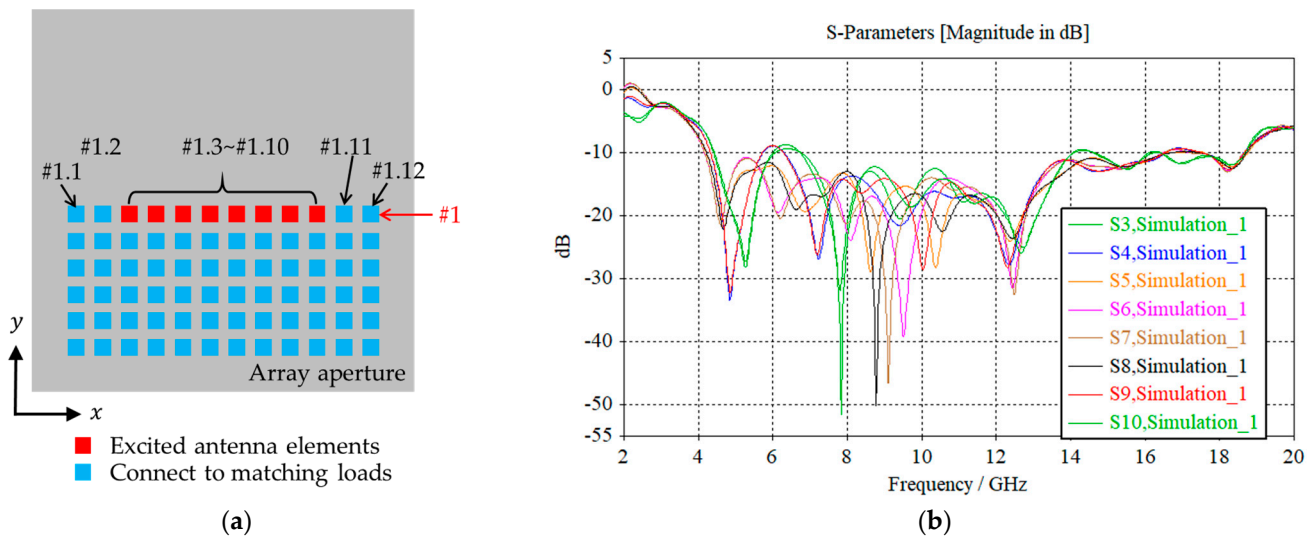


**Figure 6.** The simulated reflection coefficients of a  $12 \times 1$  linear array: (a) the schematic of the excited antenna elements and the ones of connecting to matching loads; (b) the simulated results of the reflection coefficients of the excited elements.

### 3. Prototype TCDA Construction and Measurement Results

To verify the electromagnetic characteristics of this TCDA design, a  $12 \times 12$  array prototype is manufactured. The photographs of the prototype TCDA are shown in Figure 5.

A  $150 \text{ mm} \times 150 \text{ mm}$  ground plate consists of two layers. The first layer is 3 mm thick copper layer at the bottom of the array. Following this,  $12 \times 12$  through holes are drilled on this layer. The outer conductors of the coaxial feedlines can be easily soldered to the copper layer. The inner conductors of the coaxial feedlines can go through these holes. A 5 mm thick aluminum layer is assembled on the top of the copper layer with 12 slots. It is convenient for the inner conductors of the coaxial feedlines to be soldered to the microstrip lines on the TCDA boards. These slots prevent the inner conductors and the microstrip lines being shortened by the aluminum layer. Through these slots, the copper layer can be viewed. All the 0.127 mm thick TCDA boards are vertically inserted into the aluminum plate. Since the TCDA boards are ultrathin and soft, the dielectric brackets are mounted on the aluminum plate to support the TCDA boards.

#### 3.1. The Reflection Coefficients Measurement

The simulated results of the reflection coefficients of the #1 linear array are shown in Figure 6a. Antenna elements #1.1~#1.12 belong to the #1 linear array. Furthermore, #1.1, #1.2, #1.11 and #1.12 in blue are loaded with the matching loads, and #1.3~#1.10 in red are

excited. Other elements belonging to other rows in blue are all loaded with the matching loads. The elements above the #1 linear array along the  $y$  direction are all hidden.

In Figure 6b, the reflection coefficients of the #1.3~#1.10 elements are almost uniform and all lower than  $-10$  dB from 4 GHz to 18 GHz.

The schematic diagram for the reflection coefficient measurement is shown in Figure 7a. Port1 of the vector network analyzer (VNA) in red is directly connected to the #1.6 antenna element in red to excite this element. Port2 of VNA in magenta is connected to the inputs of the power divider (PD). The eight outputs of the PD are connected to the elements in yellow to provide an active EM environment for the #1.6 element. The elements in blue mean they are connected to the matching loads. The photograph of the measurement is given in Figure 7b.

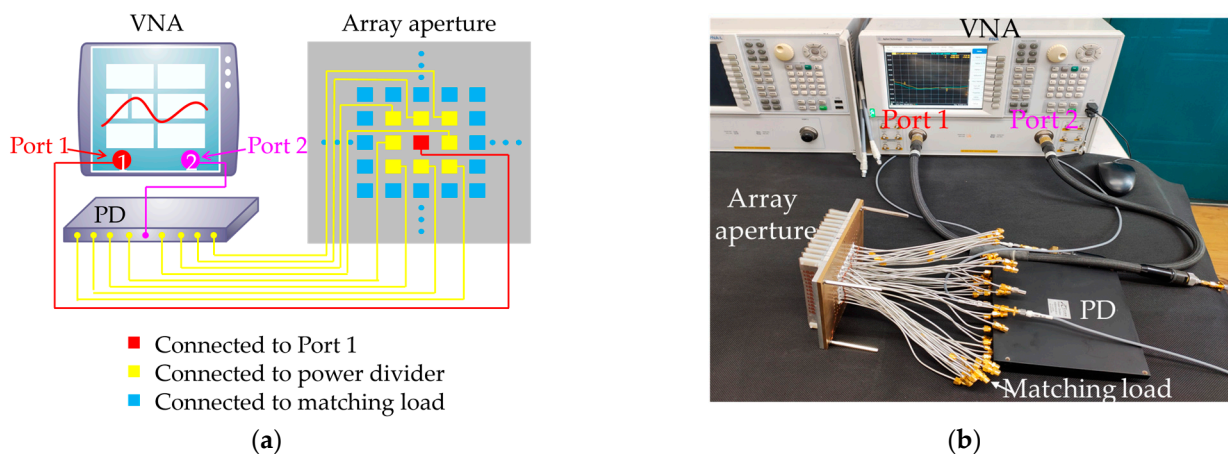


**Figure 7.** The reflection coefficient measurement. (a) The schematic diagram of the measurement. (b) The measurement setup.

The reflection coefficient of the central red radiator #1.6 is measured. The simulated and measured results are shown in Figure 8.

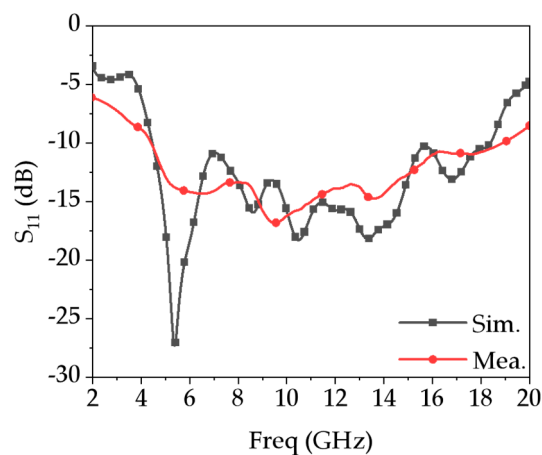


**Figure 8.** The simulated and measured results of the reflection coefficient of the excited element.

As shown in Figure 8, at 4 GHz, the active reflection coefficient  $S_{11}$  equals  $-9.19$  dB. When the frequency increases and is higher than 4.3 GHz,  $S_{11}$  decreases and is lower than  $-10$  dB. Thus, the array achieves an impressive impedance bandwidth spanning 4–18 GHz for  $S_{11} < -10$  dB.

### 3.2. The Radiation Characteristics Measurement—The Radiation Patterns of the Linear and Planar TCDAs

The radiation patterns of the linear TCDA and the planar TCDA are both tested. The schematic diagram of the excitation of the linear array in the antenna aperture is shown in Figure 9a. Only eight elements, #1.3~#1.10 of the #1 row, in the antenna aperture are excited. The schematic diagram of the feeding structure for the linear TCDA is presented in Figure 9b.

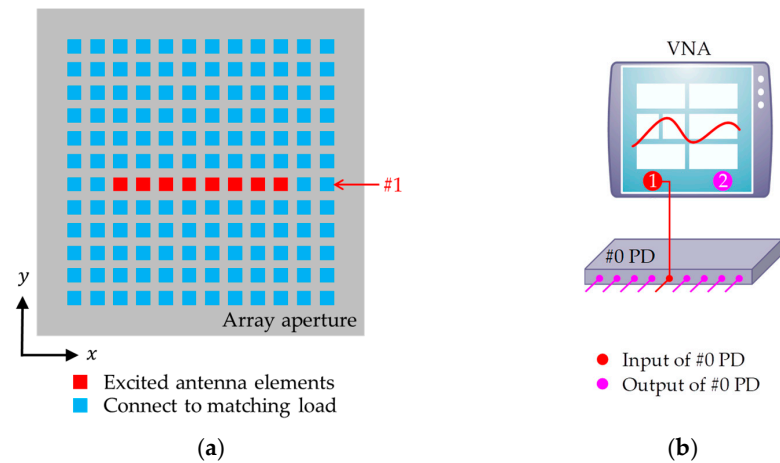


**Figure 9.** The excitation schematics of the linear array. (a) The excited antenna elements in the array aperture. (b) The cascading feeding configuration.

The E-plane and H-plane radiation patterns are separately given in Figures 10 and 11.

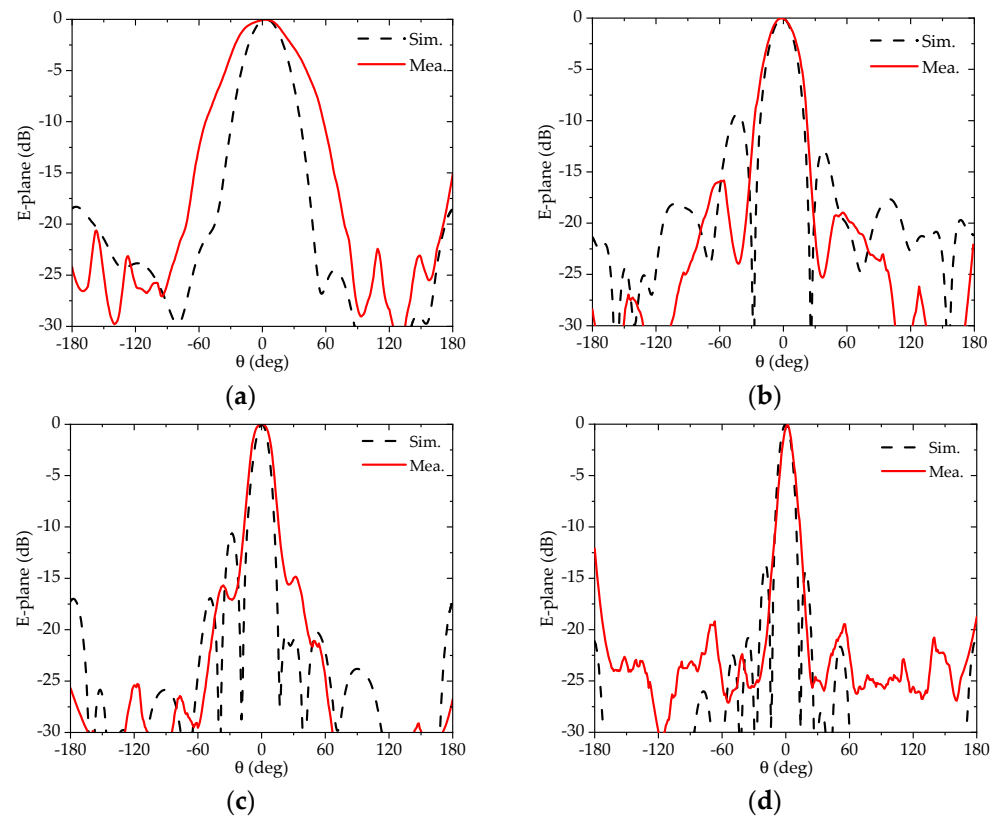


**Figure 10.** The measured E-plane radiation patterns of the linear TCDA at different frequencies. (a) at 4 GHz. (b) at 8 GHz. (c) at 12 GHz. (d) at 16 GHz.

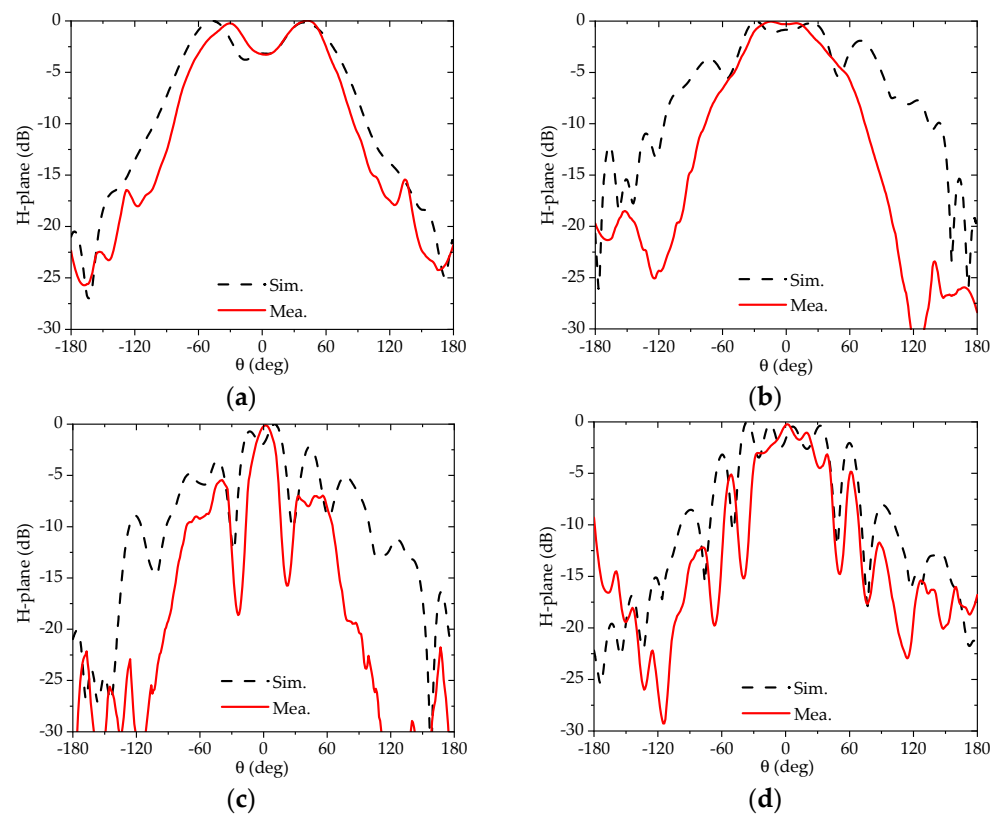


**Figure 11.** The measured H-plane radiation patterns of the linear TCDA at different frequencies. (a) at 4 GHz. (b) at 8 GHz. (c) at 12 GHz. (d) at 16 GHz.

From Figure 10, it is concluded that in the E-plane ( $xoz$  plane), #1.3~#1.10 along the  $x$  direction consists of a linear array, but in the H-plane ( $yo$ z plane), these eight antenna elements work as one element in this plane. The measured E-plane beam widths are wider than the simulated ones to some extent, especially at the lower operating frequencies such as 4 GHz and 6 GHz. As seen in Figure 11, the H-plane beams are very wide and the directivity is weak. The array elements beside the central excited row induced some electromagnetic energy and radiate as well. The excited linear array and the induced linear array generates destructive interference along some directions in space. Thus, the H-plane patterns have some dips within the main beam such as the one at 4 GHz, or just beside the main beam such as the one at 12 GHz. The directivity in the E-plane is much more obvious than the one in the H-plane.

The whole TCDA has  $12 \times 12$  elements shown in the sketch map (Figure 12a). When the edge effect is considered, the elements at the four edges are connected to the matching loads, shown in blue. The elements of the #1~#8 rows in red are connected to the outputs of eight power dividers named #1 PD to #8 PD. The eight power dividers are fed by another power divider named #0 PD. The input of #0 PD is connected directly to Port1 of the VNA. Thus, actually, there are  $8 \times 8$  excited elements.

In Figure 12b, the power dividers from #2 PD to #7 PD and many connection lines between ports of the power dividers are hidden for conciseness. The circle named "1" in red of the VNA represents the port connected to the input port of #0 PD in red. The output ports of #0 PD in red are connected to the input ports from #1 PD to #8 PD in red. The eight output ports of each divider from #1 PD to #8 PD in magenta are connected to the antenna elements of the planar TCDA in Figure 12a.

The radiation characteristics of this  $12 \times 12$  TCDA is measured in an anechoic chamber, shown in Figure 13.

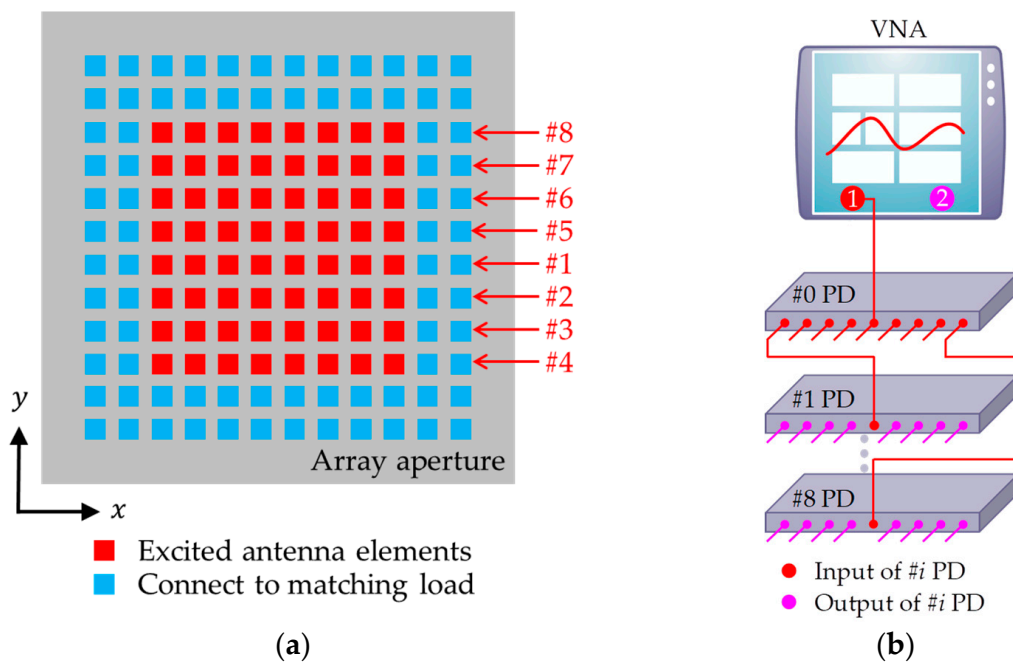


**Figure 12.** The excitation schematics of the planar array. (a) The excited antenna elements in the array aperture. (b) The cascading feeding configuration.

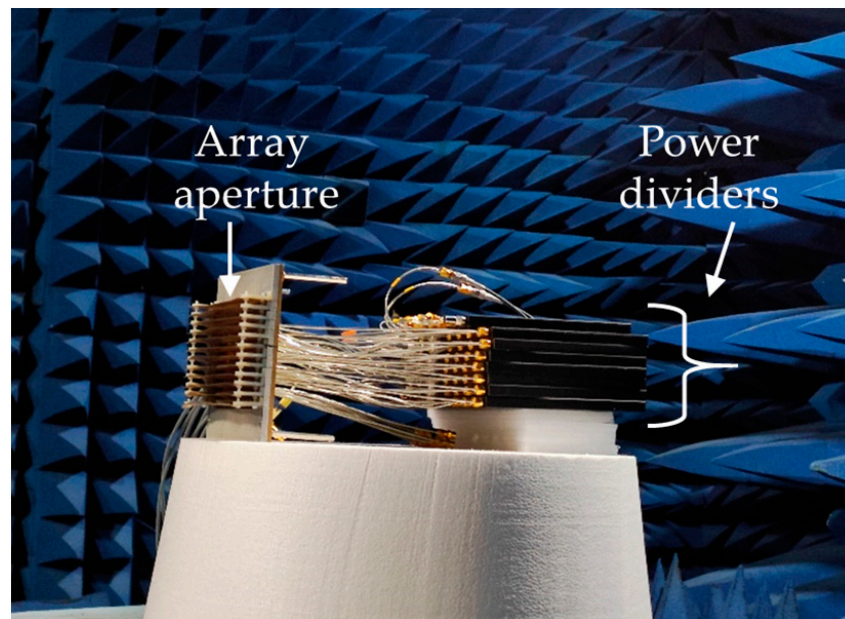


**Figure 13.** The setup of the radiation characteristics measurement.

Based on the setup above, the radiation characteristics of this TCDA are obtained. Figures 14 and 15 show the E-plane and H-plane patterns of the whole planar TCDA with  $8 \times 8$  excited elements depicted in Figure 12a.

The measured H-plane patterns of the linear TCDA in Figure 11 and the ones of the planar TCDA in Figure 15 are apparently different; the E-plane radiation-pattern characteristics of the linear TCDA and of the planar one are similar. The main beams of the planar TCDA in the H-plane at different frequencies are much narrower than the ones of the linear TCDA. The directivities of the whole planar TCDA in the H-plane greatly increase. The planar TCDA has good directivities both in the E-plane and H-plane after 8 GHz.

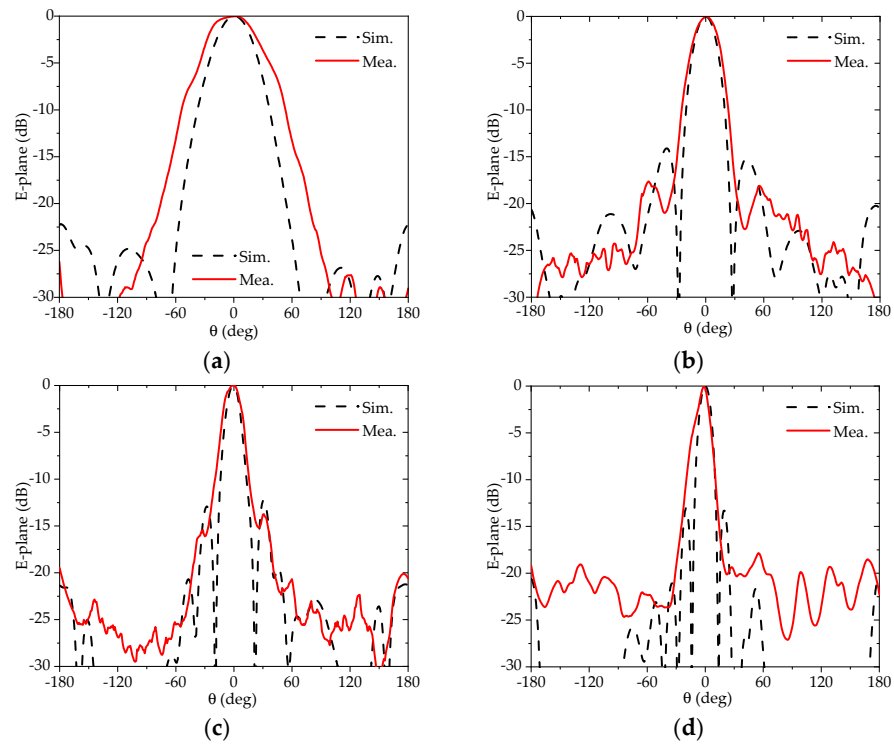


**Figure 14.** The measured E-plane patterns of the planar TCDA at different frequencies. (a) at 4 GHz, (b) at 8 GHz, (c) at 12 GHz, (d) at 16 GHz.

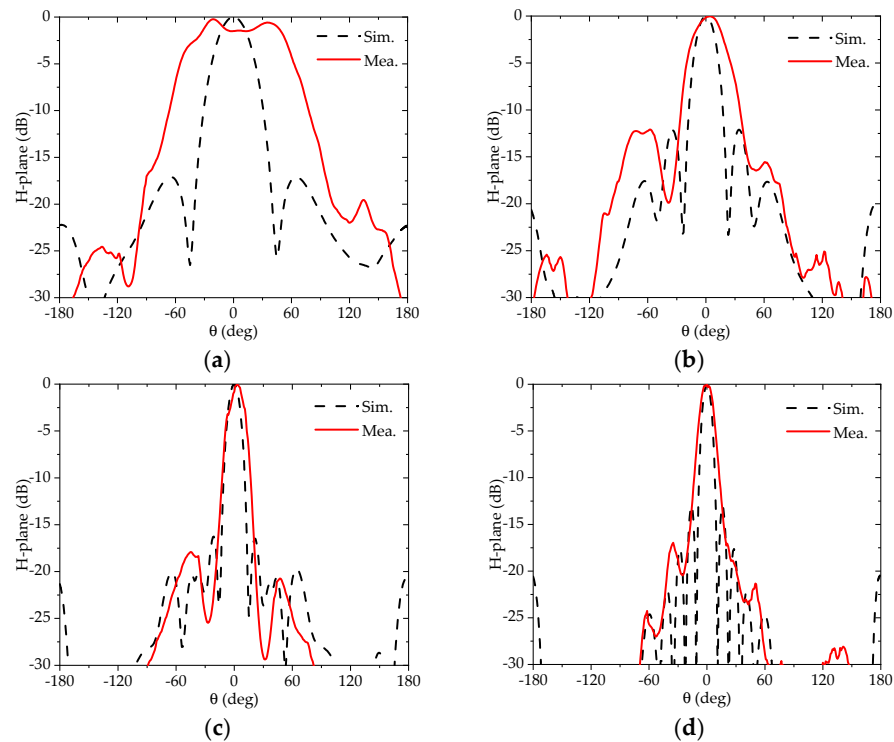


**Figure 15.** The measured H-plane patterns of the planar TCDA at different frequencies. (a) at 4 GHz, (b) at 8 GHz, (c) at 12 GHz, (d) at 16 GHz.

### 3.3. Radiation Characteristic Measurement—The Scanning Patterns of the Linear and Planar TCDAs

Eight phase-shift transmission lines (PSTLs) consist of a group of PSTLs and are connected directly to the outputs of #0 PD, as shown in Figure 16a,b.

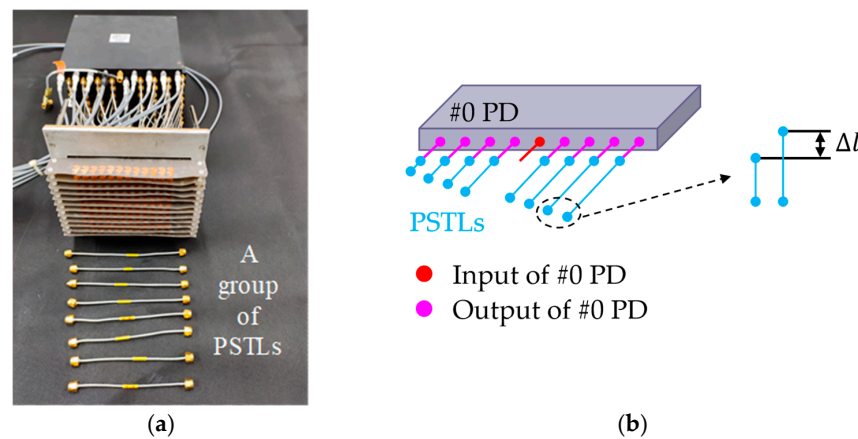


**Figure 16.** The TCDA with PSTLs. (a) The TCDA with a group of PSTLs. (b) The schematic of a group of PSTLs connected to #0 PD.

The lengths of PSTLs are different, but the differences between every neighboring PSTL  $\Delta l$  in one group of PSTLs are equivalent. When the main beam scans to a certain direction  $\theta_{deg}$  in the E-plane or H-plane, the length difference  $\Delta l$  can be obtained by the following equation:

$$\Delta l = \frac{\lambda_0 \theta_{deg}}{360} \tag{8}$$

where  $\lambda_0$  is the wavelength at the operating frequency in free space. Table 3 gives the length difference  $\Delta l$  when the beam scans to  $\theta_{deg}$ . When the lowest frequency  $f_L$  in the operating frequency band is  $f_L = 4$  GHz and the highest frequency  $f_H$  is  $f_H = 18$  GHz, the geometric mean frequency  $f_0$  equals  $f_0 = \sqrt{f_L f_H} = 8.5$  GHz. The wavelength  $\lambda_0$  is  $\lambda_0 = c/f_0 = 35.2$  mm.

**Table 3.** Dimensions of the length difference  $\Delta l$ .

$\theta_{deg} = 30^\circ$	$\Delta l = 2.9$ mm
$\theta_{deg} = 45^\circ$	$\Delta l = 4.4$ mm
$\theta_{deg} = 60^\circ$	$\Delta l = 5.8$ mm
$\lambda_0 = 35.2$ mm	$f_0 = 8.5$ GHz

The E-plane patterns and H-plane patterns when the beam scans to different directions are shown in Figures 17–19. The operating frequency is 8.5 GHz.

Considering the phase-shift error and manufacturing error, especially from the PSTLs, the measured results can be improved and achieve a better agreement with the simulated ones when actual phase shifters are applied to this planar TCDA.

### 3.4. Radiation Characteristic Measurement—The Gain of the Planar TCDA

To measure the gain of this proposed TCDA, a standard wideband horn antenna is needed and utilized in the measurement. Firstly, the electric level of this horn antenna in the main beam direction is measured in the anechoic chamber. Following this, the same measurement is performed for the TCDA. The electric level difference of these two measurements is obtained. The gain of the standard horn antenna can be found from its data sheet. Thus, the gain of the TCDA equals the gain of the standard horn antenna plus the measured electric level difference. The measured gain of the TCDA is presented in Figure 20. At 4 GHz, the measured gain is only 15 dB. From 9 GHz to 14 GHz, the differences between the measured gain and the simulated one are relatively bigger. At 18 GHz, the measured gain reaches 25 dB. Referring to the formula  $G = 4\pi\eta S/\lambda^2$  and [44] (p. 2340), the efficiency of the array is around 91%.  $G$  represents the gain,  $\eta$  is the efficiency,  $S$  is the dimension of antenna aperture and  $\lambda_0$  is the wavelength at the central frequency.

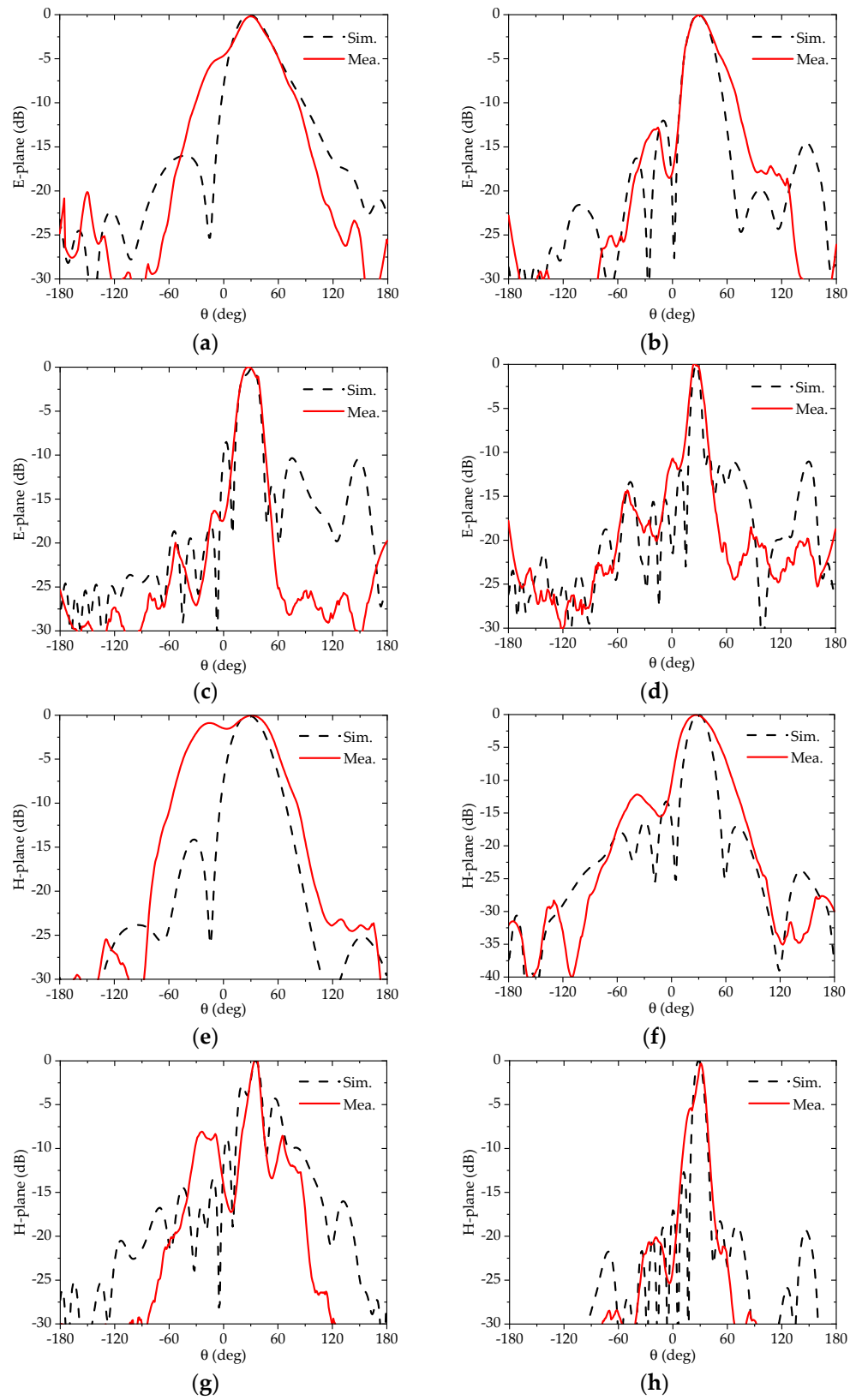


**Figure 17.** The beam scans to  $\theta_{deg} = 30^\circ$ . (a) E-plane plot at 4 GHz. (b) E-plane plot at 8 GHz. (c) E-plane plot at 12 GHz. (d) E-plane plot at 16 GHz. (e) H-plane plot at 4 GHz. (f) H-plane plot at 8 GHz. (g) H-plane plot at 12 GHz. (h) H-plane plot at 16 GHz.

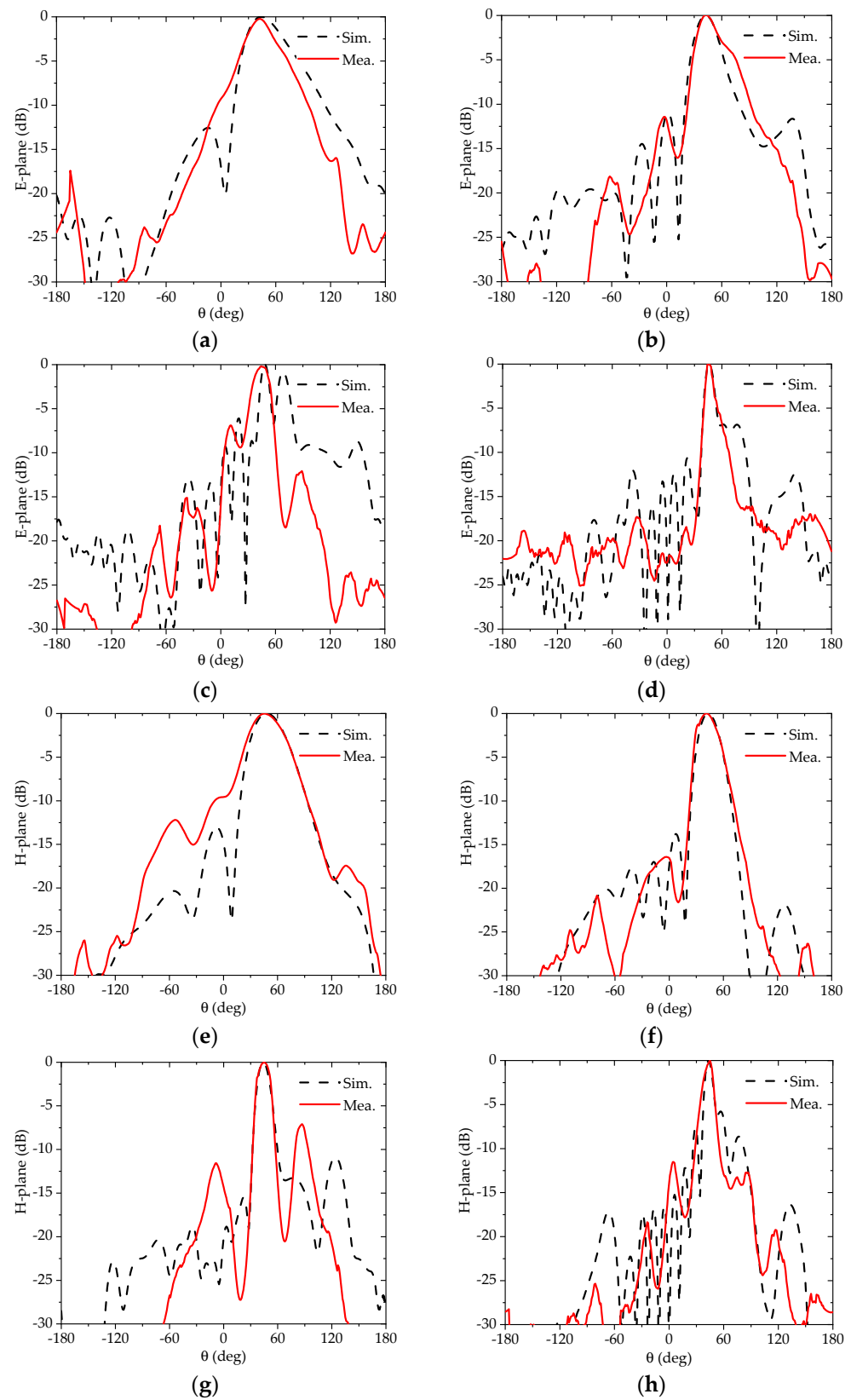


**Figure 18.** The beam scans to  $\theta_{deg} = 45^\circ$ . (a) E-plane plot at 4 GHz. (b) E-plane plot at 8 GHz. (c) E-plane plot at 12 GHz. (d) E-plane plot at 16 GHz. (e) H-plane plot at 4 GHz. (f) H-plane plot at 8 GHz. (g) H-plane plot at 12 GHz. (h) H-plane plot at 16 GHz.

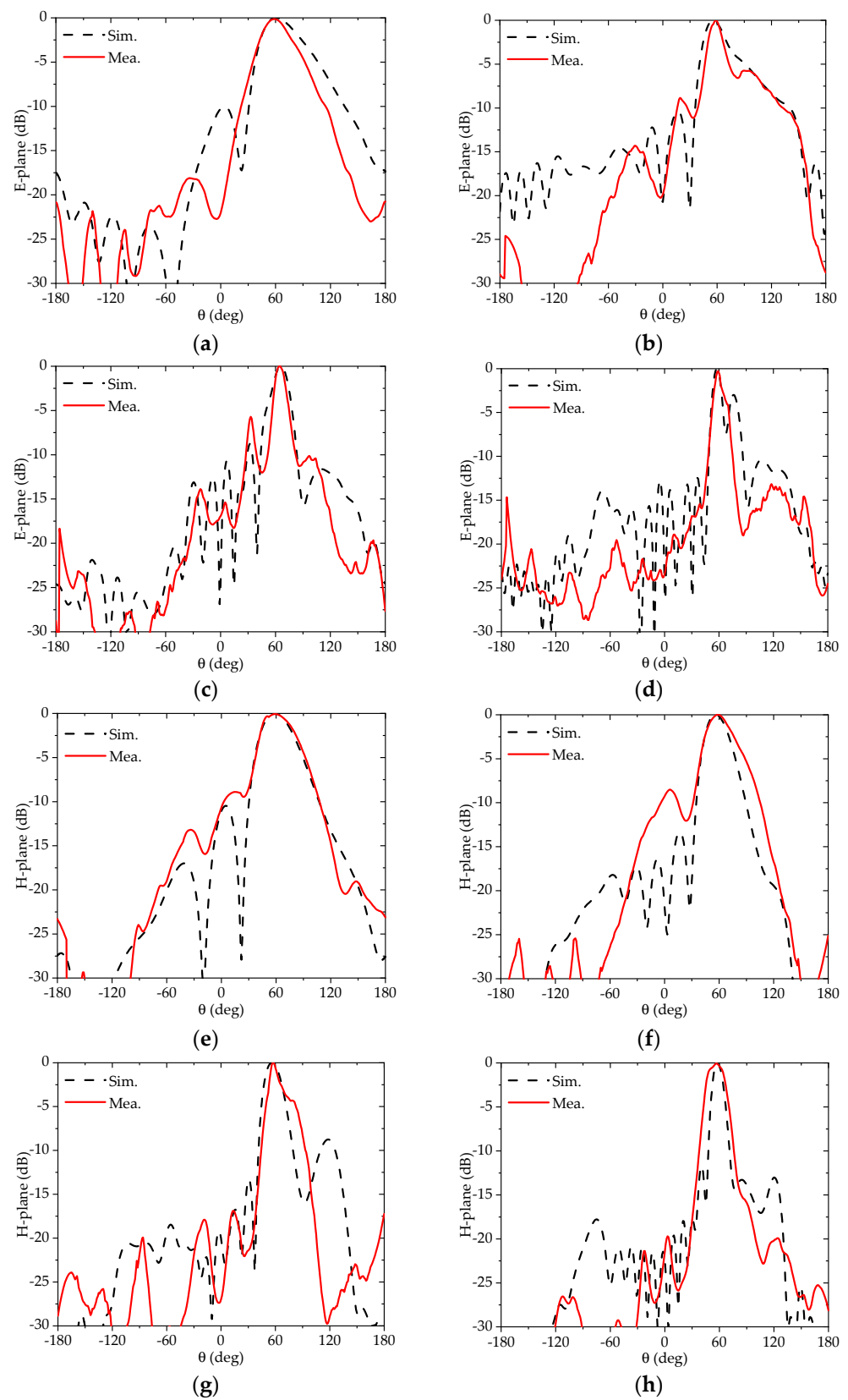


**Figure 19.** The beam scans to  $\theta_{deg} = 60^\circ$ . (a) E-plane plot at 4 GHz. (b) E-plane plot at 8 GHz. (c) E-plane plot at 12 GHz. (d) E-plane plot at 16 GHz. (e) H-plane plot at 4 GHz. (f) H-plane plot at 8 GHz. (g) H-plane plot at 12 GHz. (h) H-plane plot at 16 GHz.

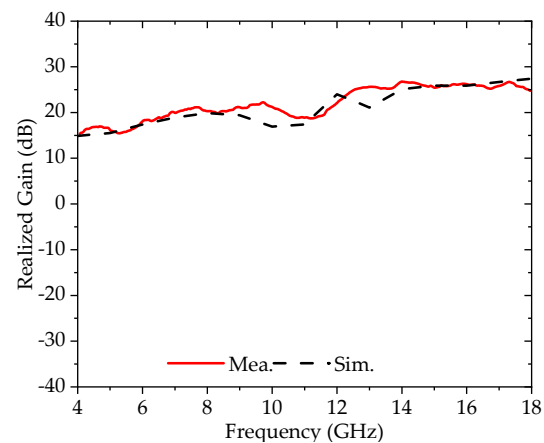


**Figure 20.** The simulated and measured gain of the planar TCDA.

Table 4 summarizes the comparison of the proposed TCDA and other reported state-of-the-art TCDAs. The work in [9,10] mainly focused on the circularly polarized TCDA, while [18] proposed an improved balanced wideband impedance transformer feed. In [19], a kind of tightly coupled balun and WAIM were utilized to improve the electromagnetic characteristics of the TCDA. Much research on the novel WAIM was undertaken in [23]. Ferrite grids were applied in [38] to expand the low end of the antenna and further reduce the overall profile.

**Table 4.** Comparison with the reported TCDAs.

Ref.	Number of Elements	Bandwidth	Feed Structure	Scanning Angle Range	Efficiency
[9]	8 × 8	3:1	Coaxial line	±45°	>70%
[10]	8 × 8	1.6:1	Corporate	Fixed-beam	>34%
[18]	8 × 8	3:1	New balun	±60°	-
[19]	8 × 8	5:1	New balun	±60°	-
[23]	11 × 11	3.7:1	Coaxial line	±75°	-
[38]	6 × 8	10:1	New balun	±60°	-
Present Work	8 × 8	4.5:1	New balun	±60°	91%

#### 4. Conclusions

In this paper, a kind of wideband tightly coupled dipole antenna (TCDA) element loaded with three capacitive pads is presented. A novel compact zigzagging balun (CZB) for this TCDA is developed and illustrated. Its equivalent circuit model is given and its transmission characteristics are theoretically analyzed. A 12 × 12 ultra-wideband and ultrathin TCDA prototype fed by the newly CZBs is manufactured and measured. The measured reflection coefficient of the central antenna element of the whole array, the E-plane and H-plane patterns, the scanning patterns and the realized gain of the array are all presented in this paper. The simulated and measured results show good agreement in most situations. This TCDA array is a good candidate for UWB phase array applications.

**Author Contributions:** Software, S.W.; Validation, Y.M.; Data curation, Y.Y.; Writing—original draft, W.W.; Project administration, N.Y. All authors have read and agreed to the published version of the manuscript.

**Funding:** This research was funded by National Defense Science and Technology Innovation Fund of the Chinese Academy, grant number 2022-JCJQ-JJ-0230.

**Data Availability Statement:** The data that support the findings of this study are available from the corresponding author, W.W., upon reasonable request.

**Conflicts of Interest:** The authors declare no conflict of interest.

## References

1. Wheeler, H. The Radiation Resistance of an Antenna in an Infinite Array or Waveguide. *Proc. IRE* **1948**, *36*, 478–487. [[CrossRef](#)]
2. Wheeler, H.A. Simple relations derived from a phased-array antenna made of an infinite current sheet. *IEEE Trans. Antennas Propag.* **1965**, *13*, 506–514. [[CrossRef](#)]
3. Munk, B.; Taylor, R.; Durharn, T.; Croswell, W.; Pigon, B.; Boozer, R.; Brown, S.; Jones, M.; Pryor, J.; Ortiz, S.; et al. A low-profile broadband phased array antenna. In Proceedings of the IEEE Antennas and Propagation Society International Symposium, Columbus, OH, USA, 22–27 June 2003; Volume 2, pp. 448–451.
4. Tan, Q.; Fan, K.; Yu, W.; Yu, Y.; Luo, G.Q. A Broadband Circularly Polarized Planar Antenna Array Using Magneto-Electric Dipole Element with Bent Strips for Ka-Band Applications. *IEEE Antennas Wirel. Propag. Lett.* **2022**, *22*, 39–43. [[CrossRef](#)]
5. Wang, S.-F.; Xie, Y.-Z.; Qiu, Y.-X. A Kind of Tightly Coupled Array with Non-Uniform Short-Circuited Branches for the Radiation of UWB Pulses. *IEEE Trans. Antennas Propag.* **2023**, *71*, 2259–2267. [[CrossRef](#)]
6. Hamza, M.; Zekios, C.L.; Georgakopoulos, S.V. A Low Profile Planar Dual-Polarized Tightly Coupled Dipole Reflectarray with 5:1 Bandwidth. *IEEE Open J. Antennas Propag.* **2022**, *3*, 958–969. [[CrossRef](#)]
7. Kim, S.; Nam, S. A Novel Reflection-Type Polarization Converter Design Using Connected Orthogonal Tightly Coupled Dipole Arrays. *IEEE Access* **2022**, *10*, 52116–52125. [[CrossRef](#)]
8. Li, Y.; Xiao, S.; Wang, B.-Z. A Wideband Circularly Polarized Connected Parallel Slot Array in the Presence of a Backing Reflector. *IEEE Access* **2020**, *8*, 26517–26523. [[CrossRef](#)]
9. Zhao, M.Y.; Zhu, Y.J.; Wang, T.; Li, T.P.; Xiao, B.L.; Niu, F.L.; Lei, X. A wideband scanning circularly polarized array antenna based on the shorted transmission line model. *IEEE Access* **2022**, *10*, 78493–78501. [[CrossRef](#)]
10. Zhang, T.-L.; Chen, L.; Moghaddam, S.M.; Zaman, A.U.; Yang, J. Millimeter-Wave Ultrawideband Circularly Polarized Planar Array Antenna Using Bold-C Spiral Elements with Concept of Tightly Coupled Array. *IEEE Trans. Antennas Propag.* **2020**, *69*, 2013–2022. [[CrossRef](#)]
11. Sun, D.M.; Hao, Z.C.; Ding, C.Y.; Liu, R.J.; Guo, Z.J.; Yin, H.Y. A Low-Profile Ultra-Wideband and Wide-Scanning Phased Array for UHF Applications. *IEEE Trans. Antennas Propag.* **2022**, *71*, 473–486. [[CrossRef](#)]
12. Wang, J.; Zhou, Y.; Gao, S.; Luo, Q. An efficiency-improved tightly coupled dipole reflectarray antenna using variant-coupling-capacitance method. *IEEE Access* **2020**, *8*, 37314–37320. [[CrossRef](#)]
13. Carvalho, M.; Volakis, J.L. Deployable Rigid-Flexible Tightly Coupled Dipole Array (RF-TCDA). *IEEE Open J. Antennas Propag.* **2021**, *2*, 1184–1193. [[CrossRef](#)]
14. Kim, S.; Nam, S. Ultra-Wideband and Wide-Angle Insensitive Absorber Based on TCDA-Under-Tightly Coupled Dipole Array. *IEEE Trans. Antennas Propag.* **2021**, *69*, 5682–5690. [[CrossRef](#)]
15. Manohar, V.; Bhardwaj, S.; Venkatakrishnan, S.B.; Volakis, J.L. VHF/UHF Ultrawideband Tightly Coupled Dipole Array for CubeSats. *IEEE Open J. Antennas Propag.* **2021**, *2*, 702–708. [[CrossRef](#)]
16. Wang, J.; Zhao, X.; Ye, Y.; Liu, S. A Millimeter-Wave Ultrawideband Tightly Coupled Dipole Array Antenna for Vehicle Communication. *IEEE Antennas Wirel. Propag. Lett.* **2022**, *21*, 2135–2139. [[CrossRef](#)]
17. Moghaddam, S.M.; Yang, J.; Zaman, A.U. Fully-Planar Ultrawideband Tightly-Coupled Array (FPU-TCA) With Integrated Feed for Wide-Scanning Millimeter-Wave Applications. *IEEE Trans. Antennas Propag.* **2020**, *68*, 6591–6601. [[CrossRef](#)]
18. Johnson, A.D.; Manohar, V.; Venkatakrishnan, S.B.; Volakis, J.L. Optimized Differential TCDA (D-TCDA) With Novel Differential Feed Structure. *IEEE Open J. Antennas Propag.* **2021**, *2*, 464–472. [[CrossRef](#)]
19. Wang, B.; Yang, S.; Chen, Y.; Qu, S.; Hu, J. Low Cross-Polarization Ultrawideband Tightly Coupled Balanced Antipodal Dipole Array. *IEEE Trans. Antennas Propag.* **2020**, *68*, 4479–4488. [[CrossRef](#)]
20. Islam, R.; Carvalho, M.; Venkatakrishnan, S.B.; Volakis, J.L. Packable and Readily Deployable Tightly Coupled Dipole Array (TCDA) With Integrated Planar Balun. *IEEE Open J. Antennas Propag.* **2022**, *3*, 1206–1217. [[CrossRef](#)]
21. Ma, Y.; Yang, S.; Chen, Y.; Qu, S.-W.; Hu, J. Sparsely Excited Tightly Coupled Dipole Arrays Based on Irregular Array Techniques. *IEEE Trans. Antennas Propag.* **2020**, *68*, 6098–6108. [[CrossRef](#)]
22. Lv, X.; Zhang, Y.; Shi, Q.; Temiz, M.; El-Makadema, A. A Dual Slant-Polarized Cylindrical Array of Tightly Coupled Dipole Antennas. *IEEE Access* **2022**, *10*, 30858–30869. [[CrossRef](#)]
23. Jiang, Z.; Xiao, S.; Yao, Z.; Wang, B.Z. A planar ultrawideband wide-angle scanning array loaded with polarization-sensitive frequency-selective surface structure. *IEEE Trans. Antennas Propag.* **2020**, *68*, 7348–7357. [[CrossRef](#)]
24. Hu, C.; Wang, B.Z.; Sun, B.F.; Wang, R.; Xiao, S.; Tong, S.Q.; Ding, X. A wide-band self-complementary tightly-coupled dipole array with  $\pm 80^\circ$  scanning range in the E plane. *IEEE Access* **2020**, *8*, 151316–151324. [[CrossRef](#)]
25. Zhang, Z.; Wang, B.; Yang, F.; Chen, Y.; Qu, S.W.; Hu, J.; Yang, S. Conical Conformal Tightly Coupled Dipole Arrays Co-Designed with Low-Scattering Characteristics. *IEEE Trans. Antennas Propag.* **2022**, *70*, 12352–12357. [[CrossRef](#)]
26. Hussain, S.; Qu, S.W.; Zhou, W.L.; Zhang, P.; Yang, S. Design and fabrication of wideband dual-polarized dipole array for 5G wireless systems. *IEEE Access* **2020**, *8*, 65155–65163. [[CrossRef](#)]

27. Zhang, Z.; Huang, M.; Chen, Y.; Qu, S.W.; Hu, J.; Yang, S. In-band scattering control of ultra-wideband tightly coupled dipole arrays based on polarization-selective metamaterial absorber. *IEEE Trans. Antennas Propag.* **2020**, *68*, 7927–7936. [[CrossRef](#)]
28. Sun, J.X.; Cheng, Y.J.; Fan, Y. Planar ultra-wideband and wide-scanning dual-polarized phased array with integrated coupled-marchand balun for high polarization isolation and low cross-polarization. *IEEE Trans. Antennas Propag.* **2021**, *69*, 7134–7144. [[CrossRef](#)]
29. Jiang, Z.; Xiao, S.; Wang, B.-Z. A Low-Cost Light-Weight Ultrawideband Wide-Angle Scanning Tightly Coupled Dipole Array Loaded with Multilayer Metallic Strips. *IEEE Access* **2021**, *9*, 24975–24983. [[CrossRef](#)]
30. Hu, C.H.; Wang, B.Z.; Gao, G.F.; Wang, R.; Xiao, S.Q.; Ding, X. Conjugate impedance matching method for wideband and wide-angle impedance matching layer with 70° scanning in the H-plane. *IEEE Antennas Wirel. Propag. Lett.* **2020**, *20*, 63–67. [[CrossRef](#)]
31. Hu, C.H.; Wang, B.Z.; Wang, R.; Xiao, S.Q.; Ding, X. Ultrawideband, wide-angle scanning array with compact, single-layer feeding network. *IEEE Trans. Antennas Propag.* **2019**, *68*, 2788–2796. [[CrossRef](#)]
32. Kim, S.; Nam, S. Characteristics of TCDA With Polarization Converting Ground Plane. *IEEE Trans. Antennas Propag.* **2020**, *69*, 2359–2364. [[CrossRef](#)]
33. Tang, H.; Zheng, B.; An, S.; Li, H.; Haerinia, M.; Fowler, C.; Zhang, H. A Broadband High-Efficiency Dipole Array Based on Frequency Selective Surface and Integrated Feeding Structure. *IEEE Open J. Antennas Propag.* **2021**, *2*, 1087–1097. [[CrossRef](#)]
34. Quan, X.; Cao, Z.; Zhou, H.; Zhu, S.; Deng, G.; Xu, C. Common-Mode Resonance Suppressing Surface for Tightly Coupled Array. *IEEE Trans. Antennas Propag.* **2022**, *70*, 12358–12363. [[CrossRef](#)]
35. Kim, S.; Nam, S. Compact Ultrawideband Antenna on Folded Ground Plane. *IEEE Trans. Antennas Propag.* **2020**, *68*, 7179–7183. [[CrossRef](#)]
36. Johnson, A.D.; Zhong, J.; Venkatakrishnan, S.B.; Alwan, E.A.; Volakis, J.L. Phased Array with Low-Angle Scanning and 46:1 Bandwidth. *IEEE Trans. Antennas Propag.* **2020**, *68*, 7833–7841. [[CrossRef](#)]
37. Carvalho, M.; Johnson, A.D.; Alwan, E.A.; Volakis, J.L. Semi-Resistive Approach for Tightly Coupled Dipole Array Bandwidth Enhancement. *IEEE Open J. Antennas Propag.* **2020**, *2*, 110–117. [[CrossRef](#)]
38. Wang, B.; Yang, S.; Zhang, Z.; Chen, Y.; Qu, S.; Hu, J. A Ferrite-Loaded Ultralow Profile Ultrawideband Tightly Coupled Dipole Array. *IEEE Trans. Antennas Propag.* **2021**, *70*, 1965–1975. [[CrossRef](#)]
39. Robinson, E.D.; Rappaport, C.M. A Lossy Transmission Line Model for the Scan Impedance of the Infinite Dipole Array. *IEEE Open J. Antennas Propag.* **2022**, *3*, 1242–1252. [[CrossRef](#)]
40. Yang, F.; Wang, B.; Chen, Y.; Qu, S.; Yang, S. An Effective Optimization Methods for the Suppression of Edge Effects in Ultrawideband Tightly Coupled Antenna Arrays. *IEEE Trans. Antennas Propag.* **2022**, *70*, 11639–11652. [[CrossRef](#)]
41. Zhou, W.; Chen, Y.; Yang, S. Efficient Design of Tightly Coupled Dipole Array Using an Equivalent Circuit-Based Approach. *IEEE Access* **2020**, *8*, 14013–14023. [[CrossRef](#)]
42. Doane, J.P.; Sertel, K.; Volakis, J.L. A Wideband, Wide Scanning Tightly Coupled Dipole Array with Integrated Balun (TCDA-IB). *IEEE Trans. Antennas Propag.* **2013**, *61*, 4538–4548. [[CrossRef](#)]
43. Cheng, D.K. Theory and applications of transmission lines. In *Field and Wave Electromagnetics*, 2nd ed.; Tsinghua University Press Limited: Beijing, China, 2020; pp. 429–435.
44. Bah, A.O.; Qin, P.Y.; Ziolkowski, R.W.; Guo, Y.J.; Bird, T.S. A Wideband Low-Profile Tightly Coupled Antenna Array with a Very High Figure of Merit. *IEEE Trans. Antennas Propag.* **2019**, *67*, 2332–2343. [[CrossRef](#)]

**Disclaimer/Publisher’s Note:** The statements, opinions and data contained in all publications are solely those of the individual author(s) and contributor(s) and not of MDPI and/or the editor(s). MDPI and/or the editor(s) disclaim responsibility for any injury to people or property resulting from any ideas, methods, instructions or products referred to in the content.